Article

Promoting Molecular Exchange on Rare-Earth Oxycarbonate Surfaces to Catalyze the Water−Gas Shift Reaction

Lu-Lu Zhou, Shan-Qing Li, Chao Ma, Xin-Pu Fu, Yi-Shuang Xu, Wei-Wei Wang, Hao Dong, Chun-Jiang Jia,* Feng Ryan Wang,* and Chun-Hua Yan*

Read Online

ACCESS | 📊 Metrics & More | 📰 Article Recommendations | 🔲 Supporting Information

ABSTRACT: It is highly desirable to fabricate an accessible catalyst surface that can efficiently activate reactants and desorb products to promote the local surface reaction equilibrium in heterogeneous catalysis. Herein, rare-earth oxycarbonates ($Ln_2O_2CO_3$, where Ln = La and Sm), which have molecular-exchangeable (H_2O and CO_2) surface structures according to the ordered layered arrangement of $Ln_2O_2^{2+}$ and CO_3^{2-} ions, are unearthed. On this basis, a series of $Ln_2O_2CO_3$-supported Cu catalysts are prepared through the deposition precipitation method, which provides excellent catalytic activity and stability for the water−gas shift (WGS) reaction. Density functional theory calculations combined with systematic experimental character-izations verify that H_2O spontaneously dissociates on the surface of $Ln_2O_2CO_3$ to form hydroxyl by eliminating the carbonate through the release of CO_2. This interchange efficiently promotes the WGS reaction equilibrium shift on the local surface and prevents the carbonate accumulation from hindering the active sites. The discovery of the unique layered structure provides a so-called "self-cleaning" active surface for the WGS reaction and opens new perspectives about the application of rare-earth oxycarbonate nanomaterials in C1 chemistry.
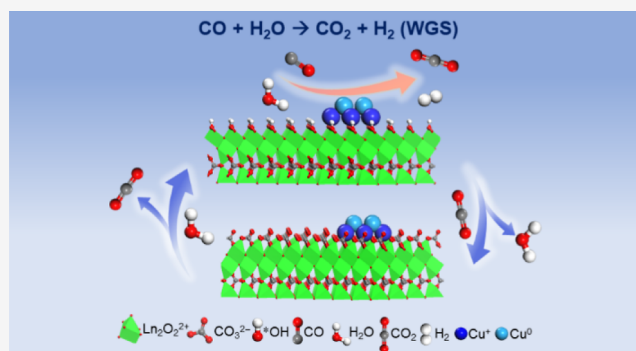
1. INTRODUCTION

In heterogeneous catalysis, it is of significant essentiality to accelerate the reaction process through designing the active catalyst surface to promote the activation of reactant molecules and favor the desorption of product molecules.[1−3] There is a dynamic equilibrium during the catalytic reaction between the reactants and products on the surface of catalysts; therefore, promoting the equilibrium shift based on Le Chatelier's principle on the local surface is highly imperative.[4,5] For decades, a widely concerned issue is whether the catalyst configuration is conducive to the adsorption and activation of reactants,[6−8] while the desorption of products and the exchange between the reactant dissociates and product adsorbates to boost the equilibrium movement is relatively less investigated.[9] Accordingly, fabricating an accessible and efficient catalyst surface that combines the advantages of efficacious dissociation of the reactant and desorption of the product is of great significance.

The WGS reaction is a crucial industrial process for hydrogen production, which is a key route to provide sustainable energy. Thus, it is vital to facilitate the forward movement of the reaction.[10−13] It is widely known that there is competitive adsorption of CO_2 and H_2O molecules on the surface of the catalysts for the WGS reaction, and $H_2O$ dissociation is generally regarded as the rate-determining step.[14−16] Thus, achieving an effective circulation of CO_2 and H_2O in the micro-reaction interface space and optimizing the local equilibrium concentration of each molecule involved in the reaction play the key role in increasing the reaction rate. In the past decades, oxide materials, including CeO_2,[12,16,17] FeO_x,[10,11,18] TiO_2,[9,15,19] and so forth, have been commonly employed as the matrix for the supported catalysts. However, owing to the formation of carbonate species, CO_2 is not discharged effectively. In addition, the accumulation of surface carbonates blocks the active sites, which has always been a tough issue.[20−23] Accordingly, designing and fabricating an ideal catalyst that separates the H_2O/CO adsorption site and the CO_2 desorption site is the optimal solution.

Our strategy lies in a facile and available conversion between the hydroxyl groups dissociating from the reactant H_2O and the inherent carbonate layer on the catalyst surface, preventing CO_2-forming carbonate species from blocking the active site. Those structures can be found in light rare-earth oxycarbonates
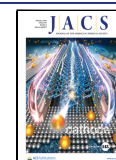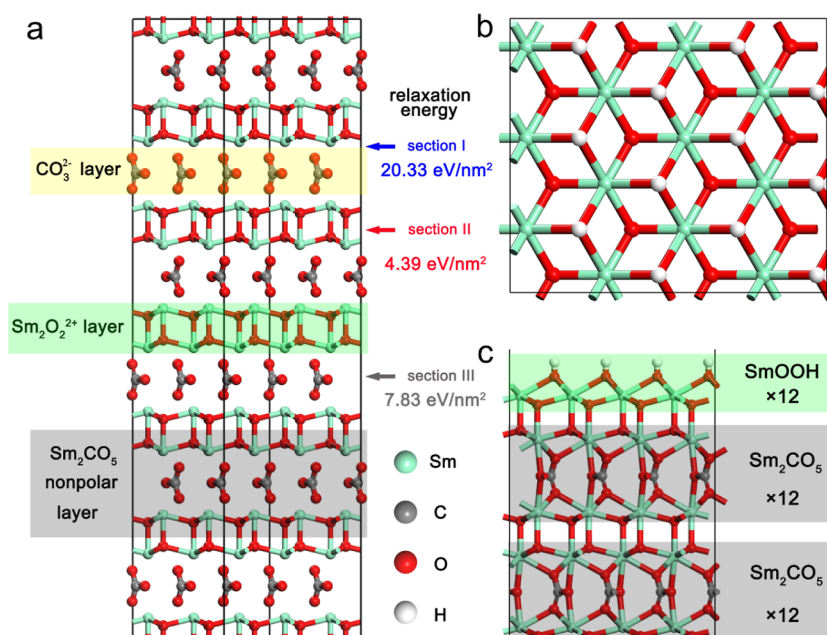
Figure 1. Structure of $Sm_2O_2CO_3$ calculated by DFT. (a) Layer structure of the $Sm_2O_2CO_3$ supercell. The Sm—O bonds are hidden in order to see the layering principle better. The $Sm_2O_2^{2+}$ and CO_3^{2-} layers are parallel to the {001} plane. The calculations suggest that section II is the advantaged position when exposed crystal surfaces are generated from the crystal $Sm_2O_2CO_3$. (b) Top view of the hydroxylated {001} $Sm_2O_2CO_3$ surface (the inner atoms are concealed). (c) Main view of the hydroxylated {001} $Sm_2O_2CO_3$ surface, which contains two complete $Sm_2O_2CO_3$ layers and one hydroxylated $Sm_2O_2^{2+}$ layer.

($Ln_2O_2CO_3$, Ln = La, Sm, etc) with a hexagonal crystal phase, which demonstrate the layered structure that the carbonate groups (CO_3^{2-}) arranged between Ln—O bilayers ($Ln_2O_2^{2+}$). As shown in Figure 1a, such a structure provides a convenient surface for the exchange of molecules (i.e., CO_2 and H_2O).[24] In addition, as a favorable metal for the adsorption of CO molecules, Cu is often used as the active metal to catalyze the WGS reaction. Hence, $Ln_2O_2CO_3$ may have the unheeded potential for catalyzing the WGS reaction, in which the $Ln_2O_2^{2+}$ layer adsorbs H_2O and then displaces the CO_3^{2-} layer to release CO_2. In this work, the $Ln_2O_2CO_3$ (Ln = La and Sm) is prepared by a controlled hydrothermal approach. Cu species are subsequently loaded on the surface of $Ln_2O_2CO_3$ through the deposition−precipitation process. The as-prepared 5Cu/ $Sm_2O_2CO_3$ catalyst exhibits excellent activity, following a reaction rate of 1711 μmol_{CO} g_{Cu}^{-1} s^{-1} at 300 °C, which is at least nearly 1 order of magnitude higher than other previously reported copper-based catalysts. The combination of density functional theory (DFT) calculations and systematic experimental characterizations confirm the interchangeability of H_2O and CO_2 through the exchange of hydroxyl and carbonate on the surface of $Ln_2O_2CO_3$, which is in favor of H_2O dissociation and CO_2 desorption while giving impetus to the equilibrium shifting of the WGS reaction. Meanwhile, the uniformly dispersed Cu^+ species on the $Ln_2O_2CO_3$ surface promote the impactful adsorption of CO molecules. The use of $Ln_2O_2CO_3$ with the layered structure as a catalyst support provides a new strategy for the fabrication of highly active catalysts for the WGS reaction and opens new opportunities in C1 chemistry, such as CH_4 combustion, CO_2 reduction, and methanol synthesis.

2. EXPERIMENTAL METHODS

2.1. Catalyst Preparation. *2.1.1. Preparation of the Samarium Oxycarbonate Support.* The $Sm_2O_2CO_3$ nanorods (NRs) were

synthesized by a modified hydrothermal method.[25] Typically, 18 mmol of $Sm(NO_3)_3\cdot6H_2O$ were dissolved in 360 mL of deionized water. Then, the pH of the solution was adjusted to 12 by the addition of 10 wt % NaOH solution. Next, the mixed solution was moved into several 100 mL stainless-steel Teflon-lined autoclaves and reacted on a temperature program of 120 °C for 12 h. The obtained mixture was washed three times with deionized water and once with ethanol, and then dried at 80 °C for 3 h. The obtained product was calcined at 450 °C for 4 h in the tube furnace.

2.1.2. Preparation of the Lanthanum Oxycarbonate Support. The $La_2O_2CO_3$ nanorods (NRs) were synthesized by the hydrothermal method.[26] First, 14.4 g of NaOH dissolved in 40 mL deionized water was separately loaded into six 100 mL Teflon bottles prepared in advance and stirred for 15 min. Then, 1.3 g of $La(NO_3)_3\cdot6H_2O$ was dissolved in 20 mL of deionized water. The solution was added to the above NaOH solution and continuously stirred for another 15 min. Then, the mixed solution was moved to six stainless-steel autoclaves and reacted on a temperature program of 100 °C for 24 h. The products were divided by centrifugation, washed with deionized water and ethanol, and then, the precipitates were dried overnight at 70 °C in an oven and calcined at 450 °C for 4 h in a tube furnace.

2.1.3. Preparation of the Reference Alumina Support. The support of Al_2O_3 nanobelts (NBs) was also prepared by a hydrothermal method.[27] First of all, 3.22 g $Al(NO_3)_3\cdot9H_2O$ and 4.6 g $CO(NH_2)_2$ were added to the 60 mL of distilled water. Next, the above-mixed solution was loaded into a 100 mL stainless Teflon-lined autoclave and kept at 100 °C for 48 h. Next, the products were washed and centrifuged with distilled water and ethanol and dried at 80 °C for 10 h. The final samples were obtained by calcining at 600 °C for 2 h.

2.1.4. Preparation of the Reference Ceria Support. Reference support CeO_2 nanorods were synthesized in the same way as $Sm_2O_2CO_3$ nanorods, except that the precursor was replaced with $Ce(NO_3)_3\cdot6H_2O$ (7.8 g).

2.1.5. Preparation of x wt % $Cu/Sm_2O_2CO_3$ Catalysts. The x wt % $Cu/Sm_2O_2CO_3$ samples were prepared via the deposition−precipitation (DP) method.[28] To begin with, 0.5 g of the above support, $Sm_2O_2CO_3$ NRs were dissolved in 25 mL of ultrapure water under

continuous stirring. Then, 0.5 mol/L of Na_2CO_3 solution and a corresponding volume of 0.1 mol/L of $Cu(NO_3)_2 \cdot 3H_2O$ solution were added into the $Sm_2O_2CO_3$ solution simultaneously until $Cu(NO_3)_2 \cdot 3H_2O$ solution was completely dripped, and the final solution pH was 9. Next, the mixture was aged for 1 h after stirring for 30 min at RT. Then, the obtained precipitation was washed and filtered with 1 L of ultrapure water. Finally, the x wt % Cu/$Sm_2O_2CO_3$ catalysts were obtained after drying at 70 °C for 10 h.

2.1.6. Preparation of x wt % Cu/Al$_2$O$_3$ and x wt % Cu/CeO$_2$ Catalysts. The synthesis method of reference Cu/Al$_2$O$_3$ and Cu/CeO$_2$ catalysts was the same as Cu/Sm$_2$O$_2$CO$_3$ with the DP method.

2.2. Characterization of Catalysts. *2.2.1. Inductively Coupled Plasma Atomic Emission Spectroscopy.* Inductively coupled plasma atomic emission spectroscopy (ICP−AES) of copper content was performed on an IRIS Intrepid II XSP instrument.

2.2.2. Transmission Electron Microscopy. The transmission electron microscopy (TEM) and high-resolution TEM (HRTEM) images were obtained on an FEI Tecnai G^2 F20 microscope instrument working at 200 kV. The high-angle annular dark-field scanning transmission electron microscopy (HAADF-STEM) images were conducted using a JEOL ARM200F microscope, which is equipped with a probe-forming spherical-aberration corrector.

2.2.3. N$_2$-Sorption Measurement. The data was tested on a Builder SSA-4200 physisorption instrument at 77 K. The samples were pretreated at 473 K for 6 h under vacuum before the test. The specific surface area of samples was calculated by the Brunauer−Emmett−Teller method.

2.2.4. X-ray Powder Diffraction Investigations. The data was acquired on the PANalytical X'Pert3 type X-ray powder diffractometer ($\lambda_{Cu.K\alpha}$ = 0.15418 nm), which worked at 40 kV and 40 mA, and the collection time of ex situ XRD was 1 h for x wt % Cu/$Sm_2O_2CO_3$ samples and 8.5 min for reference catalysts.

2.2.5. N$_2$O Chemisorption Investigations. The data were obtained on a Builder PCSA-1000 instrument to determine the Cu dispersion. First, the samples were treated at 300 °C for 30 min and heated and reduced in the H$_2$ atmosphere until 400 °C. After that, the gas was switched to N$_2$O for 1 h at room temperature to oxidize the Cu species on the surface, and the same reduction operation was performed subsequently. The hydrogen consumptions of the two times were labeled as A_1 and A_2 and then the dispersion (D) of Cu species was calculated based on the formula of $D = 2A_2/A_1 \times 100\%$.

2.2.6. Attenuated Total Reflectance Fourier Transform Infrared Spectroscopy Investigations. The data were acquired on a Thermo-Nicolet iS50 Fourier transform infrared (FTIR) spectrometer. The acquisition spectra were collected in the range from 400 to 4000 cm^{-1} with the KBr beam splitter.

2.2.7. Temperature Programmed Reduction by Hydrogen. The data were obtained on the same Builder PCSA-1000 instrument. Before the experiments, the catalysts (50 mg) were preprocessed under air at 300 °C for 30 min and purged in pure Ar at RT. Then, the catalysts were heated to 800 °C under the 5% H$_2$/Ar atmosphere with a heating rate of 10 °C·min^{-1}.

2.2.8. Ex Situ and Quasi In Situ X-ray Photoelectron Spectrometry Investigations. The data were acquired on a Thermo Scientific ESCALAB Xi$^+$ equipped with a high-temperature reaction tank (FERMI). For the in situ test, the samples could directly enter the X-ray photoelectron spectroscopy (XPS) host through the transmission system for measurement after pretreatment.

2.2.9. In Situ FTIR Spectroscopy Investigations. The data were obtained on an ultrahigh vacuum (UHV) apparatus with an FTIR spectrometer and a multichamber UHV system. The prepared samples were preprocessed in an H$_2$ atmosphere at 300 °C for 30 min and then CO was let in with desired pressure at −143 °C.

2.2.10. In Situ Diffuse Reflectance Infrared Fourier Transform Spectroscopy Investigations. The data were acquired on a Bruker Vertex 70 FTIR spectrometer with a mercury−cadmium−telluride (MCT) detector, which worked in a liquid nitrogen atmosphere. Prior to collecting the spectra, the catalyst (30 mg) was treated with an Ar atmosphere at 300 °C for 30 min; after that, the switching experiment

of 2% CO$_2$/Ar−3% H$_2$O/Ar−2% CO$_2$/Ar was carried out, and the spectra between 1000 and 4000 cm^{-1} were collected.

2.2.11. Mutual Substitution of Hydroxyl and Carbonate on Catalyst Surface Investigations. The data was obtained on an online mass spectrometer (LC-D200M, TILON, MS). After the catalysts were treated at 300 °C during Ar gas for 30 min, there were three test modes. The first experiment was to collect CO^{16}O^{16}, CO^{16}O^{18}, and CO^{18}O^{18} signals during the cycle switching between O^{18}-labeled H$_2$O^{18} and CO$_2$; the second experiment was to collect C^{12}O$_2$ and C^{13}O$_2$ signals during the cycle switching between C^{13}-labeled C^{13}O$_2$ and H$_2$O, and the third experiment was to introduce a H$_2$O/Ar or pure Ar atmosphere on the surface of the catalysts for 3 h and then switch to pure Ar for the temperature-programed experiment (RT−800 °C). CO$_2$ signals were collected during the whole process.

2.2.12. Temperature-Programmed Surface Reaction Investigations. The data was acquired on an online mass spectrometer. The catalyst (100 mg) was activated at 300 °C for 30 min under a 5% H$_2$/Ar atmosphere, then lowered to RT in the same atmosphere, and then purged in the pure Ar atmosphere. Then, the 2% CO/3% H$_2$O/Ar atmosphere was introduced at 300 °C for 1 h, and the signals of CO, H$_2$O, CO$_2$, and H$_2$ were recorded to confirm the ratio of CO$_2$ and H$_2$ and create a real in situ WGS reaction atmosphere. Next, the sample was exposed to pure Ar at 300 °C for 120 min to remove the excess gaseous H$_2$O. Then, the H$_2$O/Ar atmosphere was introduced at 250 °C for around 100 min. During this period, the signal of H$_2$ was also recorded to determine whether H$_2$O was dissociated. After that, the high-temperature purging was continued to get rid of the gaseous H$_2$O under the Ar atmosphere, only leaving the surface hydroxyl groups. Then, the temperature was lowered to RT with the same atmosphere, and 2% CO/Ar was introduced from RT to 300 °C with a heating rate of 10 °C·min^{-1} and kept at 300 °C for 60 min; the signal from CO$_2$ and H$_2$ was collected during this period. All gas flows are 30 mL·min^{-1}.

2.2.13. DFT Calculations. The periodic structures were modeled using the Vienna ab initio simulation package.[29,30] The Perdew−Burke−Ernzerhof functional and the projector augmented-wave method were applied to the spin-unrestricted optimizations.[31,32] The plane wave cut-off energy was set to 400 eV, and the convergence criteria of structural optimization were that all the forces are smaller than 0.03 eV/Å. The composite catalyst model comprised a two-layer Sm$_2$CO$_5$ {001} slab (the bottom layer was fixed), one SmOOH layer, and four Cu atoms. The lattice parameters of the surface were a = 13.5252 Å, b = 11.7132 Å, c = 34.3707 Å, and $\alpha = \beta = \gamma = 90°$, and the chemical formula of the catalyst model was Sm$_{60}$C$_{24}$O$_{144}$H$_9$Cu$_4$. The binding force between the Cu$_4$ cluster and the surface was Sm−O−Cu chemical bonds.

2.3. Catalytic Measurements and Kinetic Tests. The activity of the catalysts was tested with a WGS reaction in a fixed-bed flow reactor. 100 mg of the sample was packed into a quartz tube and reduced with a 5% H$_2$/Ar flow at 300 °C for 30 min. For the stability test, the sample only needed 50 mg. After Ar purging, the mixture of 2% CO/10% H$_2$O/N$_2$ was introduced, where the H$_2$O was pushed in by a pump. The total gas hourly space velocity (GHSV) was 42,000 mL g^{-1} h^{-1} for reactivity and 84,000 mL g^{-1} h^{-1} for stability. We collected the concentration of outlet gases, CO and CO$_2$, from 150 to 350 °C through a Gasboard 3500 IR spectrometer. We used the CO conversion during the reaction as a standard for WGS reaction activity. The specific calculation formula is as follows

$$X_{CO}(\%) = (n_{CO}^{in} - n_{CO}^{out})/n_{CO}^{in} \times 100\% \qquad (1)$$

2.4. Reaction Order and Apparent Activation Energy. The reaction order and apparent activation energy E_a were tested with the same reactor in catalytic measurements. A suitable amount of sample was weighed to hold CO conversion rates of 5−15% at the target temperatures.

3. RESULTS AND DISCUSSION

3.1. Structure of Sm$_2$O$_2$CO$_3$ and the Ability of Its Surface to Exchange Hydroxyl and Carbonate. We first
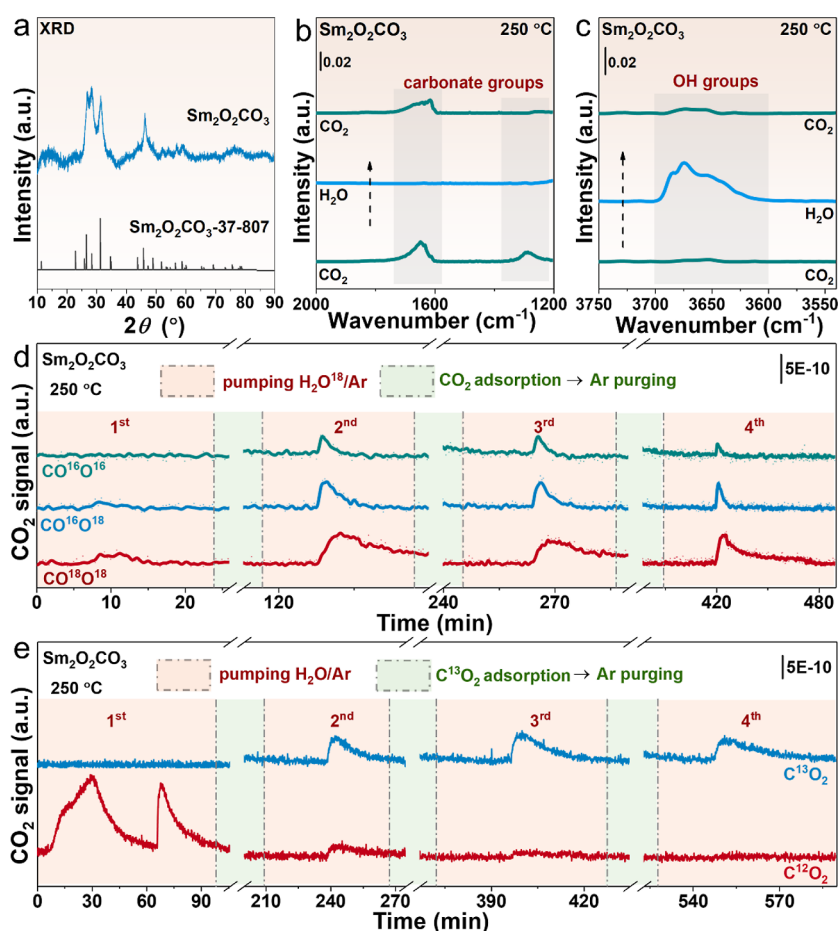
Figure 2. Substitution process of carbonate and hydroxyl species on the surface of $Sm_2O_2CO_3$. (a) XRD patterns of pristine $Sm_2O_2CO_3$; Spectral variation of (b) carbonate and (c) OH regions during the switching experiment of CO_2 and H_2O; Mass spectrometry signal variation during isotopic gas exchanges of (d) H_2O^{18} and CO_2 and (e) $C^{13}O_2$ and H_2O.

study the structure of $Sm_2O_2CO_3$ through DFT calculations and simulation models, and computational details are shown in "Computational Methods" of Supporting Information. As illustrated in Figure 1a, the $Sm_2O_2CO_3$ crystal presents an alternation of a positively charged $Sm_2O_2^{2+}$ layer and a negatively charged CO_3^{2-} layer. In order to discuss the exposed structure of the $Sm_2O_2CO_3$ surface, three potential exposed surfaces of the stable {001} facet are compared. Section I in Figure 1a is located between the $Sm_2O_2^{2+}$ and CO_3^{2-} layers. The separation of positive and negative charges leads to a higher relaxation energy of 20.33 eV/nm^2. Section II, which is situated at the center of the $Sm_2O_2^{2+}$ layer, is the most stable location for avoiding charge separation. Section III divides the carbonate ions into equal proportions, namely, half of the carbonate ions are attached to the upper surface and the other half is adsorbed on the lower surface. The simulated results show that section II is more stable than section III at 4.39 versus 7.83 eV/nm^2. From the standpoints of relaxation energy and stoichiometric proportion, the nonpolar $Sm_2O_2CO_3$ layer, shown in Figure 1b, is marked as the elementary entity of the surface model. Further calculations, shown in Figure 1c, indicated that compositions SmOOH would spontaneously arrange on the raw surface, that is, the raw surface ($Sm_2O_2CO_3 \times 24$) + 6 Sm_2O_3 + 6 H_2O → the hydroxylated surface ($Sm_2O_2CO_3 \times 24$ + SmOOH $\times 12$) ΔG = −11.66 eV. According to the configurations and energy values in Figures S1−S2 and Tables S1−S5, the hydroxylated
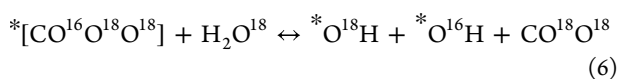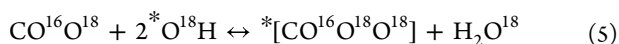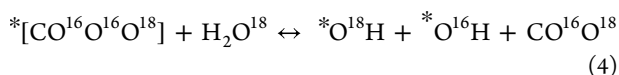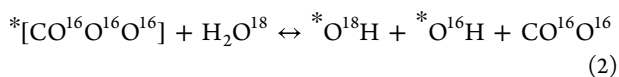
$Sm_2O_2CO_3$ surface has a lower energy value and is more stable. Therefore, the DFT calculations demonstrate that the surface of $Sm_2O_2CO_3$ is highly susceptible to H_2O, which is vital for the dissociation of H_2O and further WGS reaction.

$Sm_2O_2CO_3$ is prepared via the hydrothermal method. According to the XRD patterns (Figure 2a), hexagonal $Sm_2O_2CO_3$ is the dominant phase. Combined with multiple carbonate peaks in attenuated total reflectance FTIR (Figure S3),[33] the carbonate groups in $Sm_2O_2CO_3$ are verified. To continue exploring the ability of the $Sm_2O_2CO_3$ to dissociate H_2O, the experimental characterizations of in situ DRIFTS and mass spectrometry (MS) are employed. Figure 2b,c shows the spectral variation of carbonate and hydroxyl group regions during the gas exchanges between CO_2 and H_2O. In detail, after the introduction of CO_2 at 250 °C, two distinct peaks attributed to carbonate species appear at 1647 and 1287 cm^{-1},[20,34] which disappear almost simultaneously when switching to H_2O, while the hydroxyl groups peak appear within 3650−3700 cm^{-1}.[20,24] Notably, these surface carbonate species (Figure 2b) are different from the intrinsic CO_3^{2-} in $Sm_2O_2CO_3$ (1484 and 1370 cm^{-1}, Figure S3). More interestingly, when switching back to CO_2, the peaks of carbonate species reappeared, while the hydroxyl groups disappeared. The above results clearly display the mutual substitution between hydroxyl groups and carbonate on the surface of $Sm_2O_2CO_3$. Subsequently, as shown in Figure 2d,e, the MS data with isotopic gas exchanges also confirms the
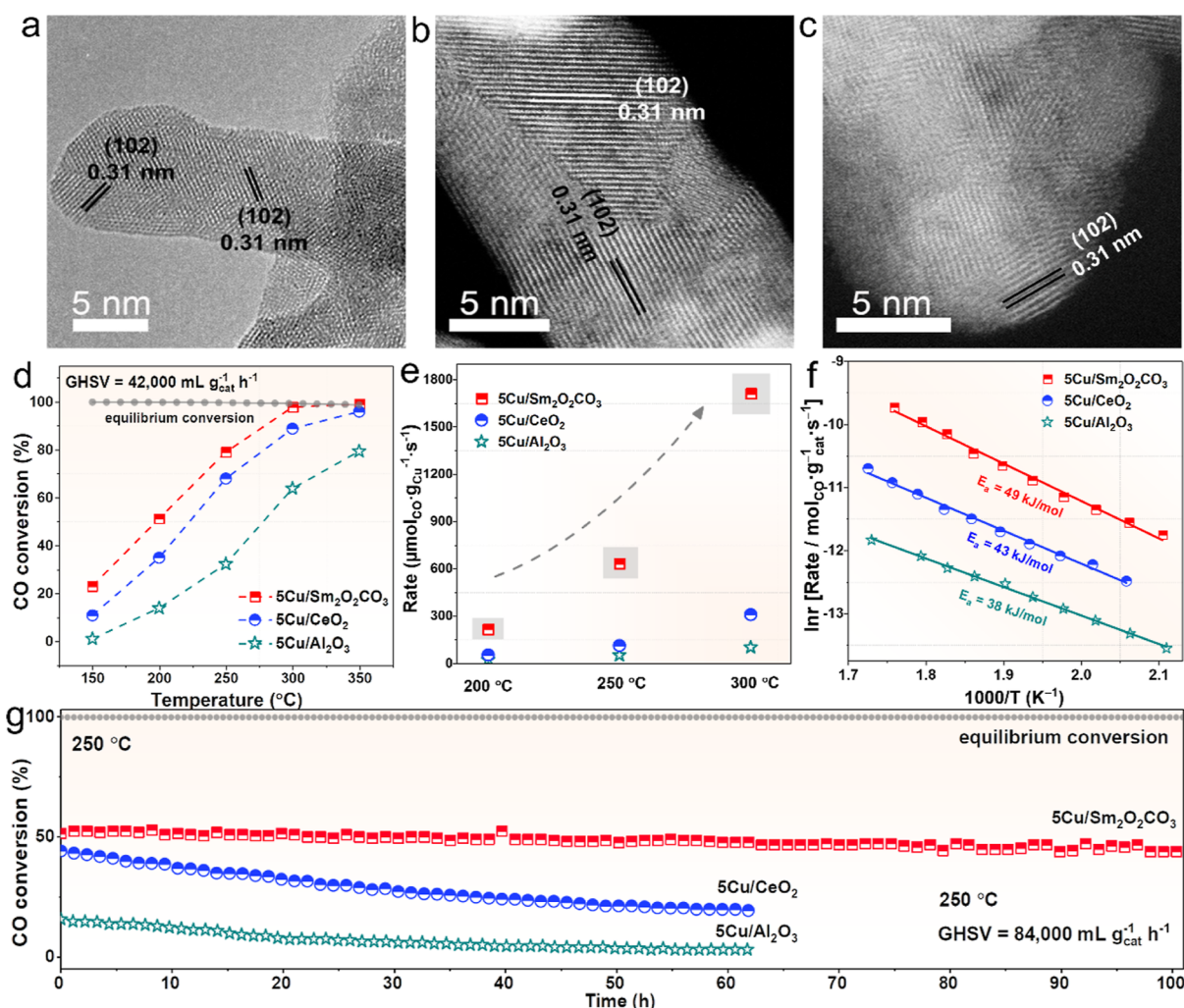
Figure 3. Morphology and catalytic performance over catalysts. (a) HRTEM and (b,c) aberration-corrected HAADF−STEM images of used 5Cu/Sm$_2$O$_2$CO$_3$ catalysts; (d) catalytic performances test (100 mg, GHSV = 42,000 mL g$_{cat}^{-1}$ h^{-1}), (e) comparison of WGS reaction rates, (f) apparent activation energy value, and (g) stability test for about 100 h of the 5Cu/Sm$_2$O$_2$CO$_3$, 5Cu/CeO$_2$, and 5Cu/Al$_2$O$_3$ catalysts.

exchange capacity. In the exchange experiment of H$_2$O^{18} and CO$_2$ on the Sm$_2$O$_2$CO$_3$ support surface, various CO$_2$ signals emerge after cleaning the surface with Ar gas and H$_2$O^{18} exposure (Figure 2d). The phenomenon is believed to be that the O^{18}H* generated by the dissociation of H$_2$O^{18} replaced the *CO$_3$ groups on the surface and successively released CO^{16}O^{16}, CO^{16}O^{18}, and CO^{18}O^{18}, corresponding surface exchange reactions are as follows eqs 2−6

$$*[CO^{16}O^{16}O^{16}] + H_2O^{18} \leftrightarrow {}^*O^{18}H + {}^*O^{16}H + CO^{16}O^{16} \quad (2)$$

$$CO^{16}O^{16} + 2\,{}^*O^{18}H \leftrightarrow {}^*[CO^{16}O^{16}O^{18}] + H_2O^{18} \quad (3)$$

$$*[CO^{16}O^{16}O^{18}] + H_2O^{18} \leftrightarrow {}^*O^{18}H + {}^*O^{16}H + CO^{16}O^{18} \quad (4)$$

$$CO^{16}O^{18} + 2\,{}^*O^{18}H \leftrightarrow {}^*[CO^{16}O^{18}O^{18}] + H_2O^{18} \quad (5)$$

$$*[CO^{16}O^{18}O^{18}] + H_2O^{18} \leftrightarrow {}^*O^{18}H + {}^*O^{16}H + CO^{18}O^{18} \quad (6)$$

Note: The carbonate and hydroxyl groups in the formula are adsorbed on the surface of the catalyst.

In order to further verify the replacement process, CO$_2$ adsorption is performed to displace hydroxyl groups and supplement the carbonate layer. After Ar purging, during the second introduction of H$_2$O^{18}, the corresponding CO$_2$ signals reappear as expected. Then, the next two rounds of the CO$_2$ adsorption experiment continue to be manipulated. Similarly, the diverse CO$_2$ signals are generated again after H$_2$O^{18} is introduced, further affirming the continuity of the replacement processes of carbonate and hydroxyl. During the introduction of H$_2$O^{18} in each cycle, the generation of the higher intensity of the labeled CO$_2$ signal also further confirms that the displaced CO$_2$-formed carbonate is efficiently replaced by the *O^{18}H generated by the dissociation of H$_2$O^{18}. In terms of the process of isotopic gas exchanges of C^{13}O$_2$ and H$_2$O (Figure 2e), C^{12}O$_2$ appears after the first pumping of H$_2$O. After that, in the next three rounds of testing, C^{13}O$_2$ is utilized to replenish the surface carbonate layer, then H$_2$O is introduced, and only the signal of C^{13}O$_2$ appears. C^{12}O$_2$ only appears in the first cycle, indicating a very efficient exchangeability of *OH to surface *CO$_3$. The abovementioned characteristics indicate that the molecular-exchangeable highway of CO$_2$ and H$_2$O is constructed on the surfaces of rare-earth oxycarbonate.

Thereafter, the MS results of the Ar-temperature-programed experiment with and without H$_2$O pretreatment are shown in

Table 1. Comparison of the Reaction Rates Over Various Catalysts

| samples	CO/H$_2$O	Cu (wt %)[a]	temperature (°C)	rate (μmol$_{CO}$ gCu^{-1} s^{-1})	ref.
5Cu/Sm$_2$O$_2$CO$_3$	1:5	3.8	300	1711	this work
5Cu/GDC (combustion)	1:2	5.0	300	74	[36]
Mg$_{0.52}$Cu$_{0.35}$Ce$_{0.13}$(G)	1:3	23.0	300	213	[37]
Mg$_{0.52}$Cu$_{0.35}$Ce$_{0.13}$	1:6	23.0	300	361	[37]
Cu$_{0.73}$Ce$_{0.23}$	1:6	44.5	300	67	[37]
Cu-in-TiO$_2$NT	N/A	2.0	300	31	[38]
CuZnAl	1:6.7	50.6	300	15	[39]
CuO/Fe$_2$O$_3$	1:1	2.4	330	167	[18]
Cu/Al−Fe	1:1	2.3	330	257	[40]
5Cu/Sm$_2$O$_2$CO$_3$	1:5	3.8	250	632	this work
Cu/CeO$_2$-NP(T)	1:1	5.1	250	219	[41]
Cu$_{10}$/SiO$_2$	1.1:1	10	250	14	[42]
Cu$_{10}$Fe$_{1-0}$/SiO$_2$	1.1:1	10	250	19	[42]
7.0CuCe-Cube-L	1:5	7	250	18	[28]
5Cu/Sm$_2$O$_2$CO$_3$	1:5	3.8	200	216	this work
CuCe−H$_2$	1:6.7	14.4	200	21	[43]
Cu/CeO$_2$-473	1:3	3.4	200	147	[17]
CMO-CP	1:2	28.1	200	10	[44]
CuO−CeO$_2$	1:3.1	6.4	200	2	[45]
CuO−Al$_2$O$_3$	1:3.1	6.4	200	38	[45]
CuO−ZnO−Al$_2$O$_3$	1:3.1	32	200	24	[45]
Cu/TiO$_2$\{001\}	1:2	11	200	20	[46]
10%Cu−Ce(La)O$_x$	1:5	10	200	21	[47]

[a]Determined by ICP-AES.

Figure S4a,b. The obvious CO$_2$ signal is generated immediately after the sample is pretreated with H$_2$O and the CO$_2$ peak at low temperature (designated as surface carbonate) vanishes during the subsequent Ar-temperature-programed process, while the peak of CO$_2$ in the high-temperature area (designated as bulk carbonate) remained stable. This is consistent with the exchange of hydroxyl and carbonate layers on the surface of Sm$_2$O$_2$CO$_3$. Furthermore, the 5Cu/Sm$_2$O$_2$CO$_3$ surface exhibits a similar *OH and *CO$_3$ exchange capacity to Sm$_2$O$_2$CO$_3$ (Figure S4c). In contrast, there is no CO$_2$ produced when H$_2$O is introduced for the reference 5Cu/Al$_2$O$_3$ catalyst (Figure S5), indicating that it does not have the exchange capability. Thus, compared with stable carbonate species on other oxide surfaces,[9,35] the accessibility of the carbonate layer on the surface of Sm$_2$O$_2$CO$_3$ provides favorable conditions for the exchange with hydroxyl. In conclusion, the combination of theory and experimental study demonstrates that the rare-earth oxycarbonates are naturally beneficial to the dissociation of H$_2$O and produce *OH for exchange with the *CO$_3$ formed by CO$_2$ adsorption, realizing the efficient circulation of reactants and product molecules, which creates favorable conditions for accelerating the progress of the WGS reaction.

3.2. Structure and Catalytic Performance of the Copper-Samarium Oxycarbonate Catalysts. After confirming the ability of the support surface to exchange hydroxyl and carbonate, systematic experimental characterizations are performed to identify the morphology and composition of the sample after loading Cu species and the performance for catalyzing the WGS reaction. The actual Cu content based on the ICP result and physical properties of the catalysts are collected in Table S6. The TEM images (Figure S6a,b) unravel that the bare Sm$_2$O$_2$CO$_3$ support presented nanorod-like morphology. Minor changes could be detected after loading 5 wt % Cu on the Sm$_2$O$_2$CO$_3$ surface by the DP method for both

fresh (Figure S6c) and used catalysts (Figure S6d). As revealed in the HRTEM and HAADF-STEM images of the used 5Cu/Sm$_2$O$_2$CO$_3$ sample (Figure 3a−c), the characteristic lattice distance with 0.31 nm belongs to the \{102\} crystal plane of the Sm$_2$O$_2$CO$_3$ matrix, and still, no Cu-related species are observed. This verifies the homogeneous distribution of Cu species on the Sm$_2$O$_2$CO$_3$ surface after the WGS reaction, indicative of the relatively stable metal−support interaction, which can also be confirmed by the EDS elemental mapping images of the used 5Cu/Sm$_2$O$_2$CO$_3$ sample in Figure S7. The XRD data of the 5Cu/Sm$_2$O$_2$CO$_3$ sample, shown in Figure S8, is well in line with the above TEM images, with only the phase of Sm$_2$O$_2$CO$_3$ for the prepared and spent catalysts, and the characteristic diffraction peaks of Cu species are invisible. However, for the spent reference 5Cu/Al$_2$O$_3$ sample, aggregated Cu particles with a diameter of ∼27 ± 9 nm are visible in the TEM and EDS elemental mapping images, in contrast to the fresh samples with clean surfaces (Figure S9). Similarly, the characteristic peak of metallic Cu is observed in the XRD patterns (Figure S10). Another reference 5Cu/CeO$_2$ catalyst is the same as 5Cu/Sm$_2$O$_2$CO$_3$, the Cu species are well dispersed from TEM images (Figure S11), and no peaks for Cu species in the XRD result (Figure S12).

The WGS reaction catalytic performance of the samples is evaluated over the tested temperature range of 150 to 350 °C. The typically irreducible Al$_2$O$_3$ and reducible CeO$_2$ are employed as reference supports for loading Cu species to confirm the superiority of the Sm$_2$O$_2$CO$_3$ support material. As shown in Figure 3d, as expected, the 5Cu/Sm$_2$O$_2$CO$_3$ catalyst exhibits the CO conversion of ∼80% at 250 °C and reaches the equilibrium conversion at 300 °C, with a GHSV of 42,000 mL g^{-1} h^{-1}, which outperformed that of Cu/CeO$_2$ (∼67%−250 °C) and Cu/Al$_2$O$_3$ (∼30%−250 °C). Meanwhile, the CO consumption rate of 5Cu/Sm$_2$O$_2$CO$_3$ is 5−6 times that of 5Cu/CeO$_2$ and 10−17 times that of 5Cu/Al$_2$O$_3$ at various
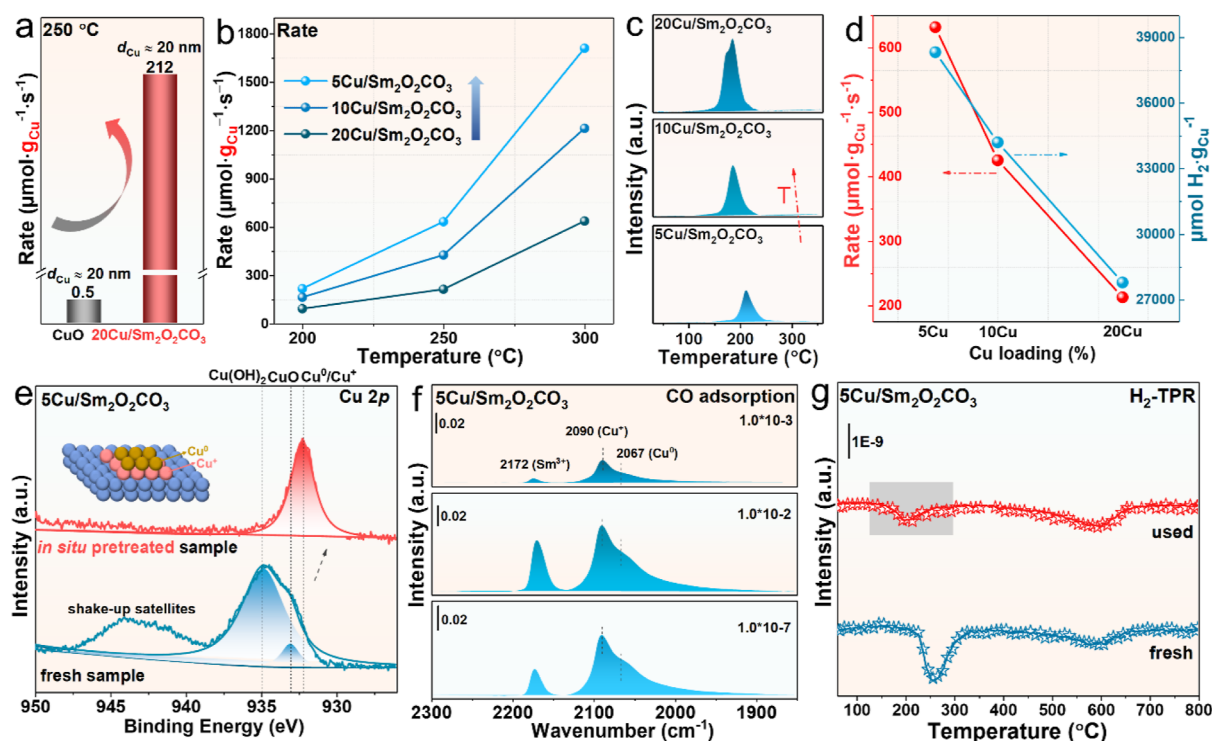
Figure 4. Identification of the active site of the $Cu/Sm_2O_2CO_3$ catalyst. (a) Reaction rates normalized by Cu weight for CuO and 20Cu/$Sm_2O_2CO_3$ samples at 250 °C; (b) reaction rates normalized by Cu weight at various temperatures and (c) TCD signals of H_2-TPR profiles over $xCu/Sm_2O_2CO_3$ (x = 5, 10 and 20) catalysts; (d) reaction rates normalized by Cu weight at 250 °C and calculation of hydrogen consumption normalized by Cu weight from H_2-TPR for $xCu/Sm_2O_2CO_3$ samples; (e) ex situ Cu $2p$ XPS spectra of fresh 5Cu/$Sm_2O_2CO_3$ catalyst and quasi in situ Cu $2p$ XPS spectra of used 5Cu/$Sm_2O_2CO_3$ catalyst; (f) in situ infrared spectra of 5Cu/$Sm_2O_2CO_3$ exposed to different CO pressures at −143 °C after H_2 pretreatment. (g) MS signals of H_2-TPR profiles of fresh and used 5Cu/$Sm_2O_2CO_3$ samples.

temperatures (Figure 3e) and is at least nearly one order of magnitude higher than that of other copper-based samples, which reported in the literature, as shown in Table 1.[17,18,28,36−47] In addition, these three catalysts demonstrate approximate apparent activation energies (E_a) but diverse prexponential factors values (A) in Figure 3f. This reflects the similar reaction mechanism of these catalysts, while the 5Cu/$Sm_2O_2CO_3$ possesses the most active sites,[48] which is in accordance with the numerous surface-active hydroxyl sites in $Sm_2O_2CO_3$, as calculated by DFT. Besides, the kinetic test shown in Figures S13 and S14 also indicates that the pre-exchanged H_2O molecules directly contributed to the generation of CO_2 via surface reaction. Furthermore, the 5Cu/$Sm_2O_2CO_3$ catalyst presents excellent long-term durability at 250 °C under the condition that the CO conversion rate is far from the equilibrium conversion rate and a higher GHSV of 84,000 mL g^{-1} h^{-1}, retaining nearly 90% of the original activity within 100 h (Figure 3g). In contrast, the 5Cu/CeO_2 and 5Cu/Al_2O_3 catalysts lose 57% and 81% of their initial activity after the 60 h stability test, respectively. Meanwhile, the apparent catalytic performance test (Figure S15) clearly indicates that the 5Cu/$Sm_2O_2CO_3$ catalyst possesses the lowest decline rates of the CO conversion rate after the introduction of CO_2 atmosphere in the catalytic system compared to the other two samples. These results reach an agreement with the abovementioned exchange process, in which the *OH generated by the dissociation of H_2O on the surface of 5Cu/$Sm_2O_2CO_3$ sufficiently exchanges the *CO_3 formed by CO_2 adsorption, promoting the local equilibrium shifting of the reaction by effectively release of CO_2. The performance characterization results of the catalysts verify the

superiority of the 5Cu/$Sm_2O_2CO_3$ catalyst, compared to conventional oxide catalysts.

3.3. Study on Reactive Cu Species for CO Adsorption. The status of Cu species is also critical for the adsorption of CO molecules in supported catalysts. To clarify the true active site of adsorption of CO in the WGS reaction, we have prepared a series of $xCu/Sm_2O_2CO_3$ (x = 5, 10, and 20) catalysts with various Cu contents. Meanwhile, bare CuO nanoparticles with diameters of ∼20 nm are controllably synthesized, which are comparable to the size of Cu particles precipitated in the 20Cu/$Sm_2O_2CO_3$ sample (Figure S16). According to the CO consumption rate normalized by Cu weight (r) of these two samples at 250 °C in Figure 4a, it clearly shows that the r value of 20Cu/$Sm_2O_2CO_3$ is much higher than that of bare CuO particles (212 vs 0.5). In addition, from the catalytic activity of $xCu/Sm_2O_2CO_3$ shown in Figure S17, the reactivity of supported catalysts has been greatly improved compared to bare support and CuO; the results suggest that the WGS reaction might occur preferentially on the interface of samples, and the interaction between the Cu and support enhances the reactivity. Furthermore, the XRD patterns (Figure S18) and the Cu dispersion experiments (Figure S19 and Table S7) reveal that the characteristic peaks of metallic Cu are more obvious, and the Cu dispersions are lower in the samples with a higher Cu content. Moreover, the reaction rate (r) normalized by Cu weight in Figure 4b exhibits that the Cu/$Sm_2O_2CO_3$ samples with lower Cu content have a higher r value, which further confirms that the small-sized Cu species with good dispersion at the interface are the better active species.
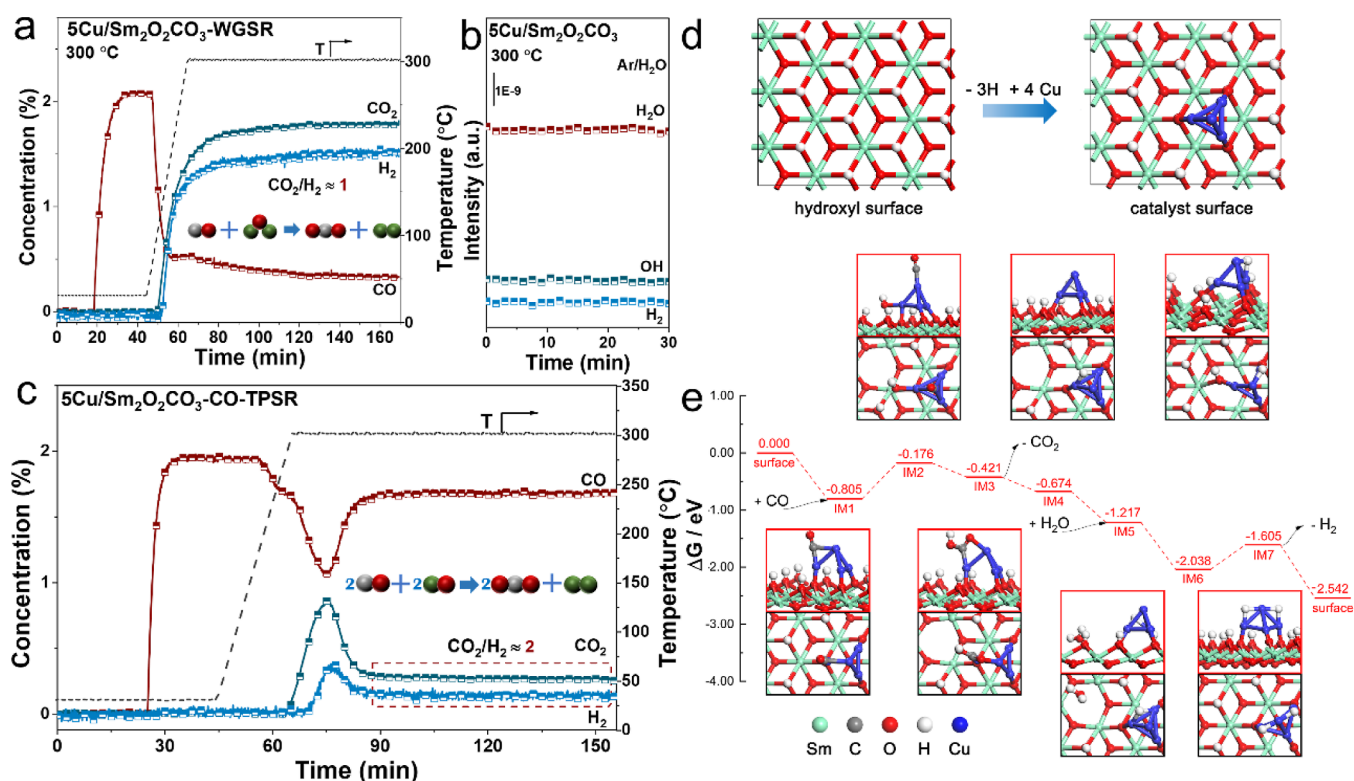
Figure 5. WGS reaction mechanism study of the $5Cu/Sm_2O_2CO_3$ catalyst. (a) In situ WGS reaction at 300 °C, (b) experiment of H_2O dissociation, (c) CO-TPSR of the catalyst, and (d) structure of catalyst surface (top view). (e) Reaction mechanism scheme of the WGS reaction. The structure diagrams with red frames are the main views of intermediate structures, and the diagrams with black frames are top views (the inner atoms are concealed). The Gibbs free energies are calculated at 250 °C, with the partial pressure of CO of 2 kPa and the partial pressure of H_2O of 10 kPa.

For the purpose of revealing the redox properties of Cu species in $xCu/Sm_2O_2CO_3$ samples, H_2-TPR is performed and shown in Figures 4c and S20. Combining the H_2-TPR results in the region in 300−800 °C (Figure S20a) and MS signal of CO_2 in $5Cu/Sm_2O_2CO_3$ catalyst during temperature programming under Ar (Figure S20b), the reduction peak below 300 °C is designated as the reduction of Cu species, and the peaks above 300 °C is designated as the decomposition of $Sm_2O_2CO_3$. Thus, the increase in reduction temperature is accompanied by a decrease in Cu loading, demonstrating the stronger interaction between Cu and support in the samples with a low Cu content (Figure 4c). Correspondingly, the Cu-normalized activity of the samples and the integrated area of peaks in H_2-TPR are negatively correlated with the Cu content as displayed in Figure 4d. Accordingly, the samples with low Cu content have more Cu species that coordinate with O species, which have preferable WGS reactivity.

Figure 4e displays the ex situ and quasi in situ Cu 2p XPS spectra of $5Cu/Sm_2O_2CO_3$ with a deconvolution by the Gaussian peak fitting method to confirm the electronic status of Cu species before and after the reaction. According to the collected spectra, the substantial part of the Cu species in the pristine sample exists in the form of $Cu(OH)_2$ located at 934.8 eV, with a modicum of CuO located at 933 eV.[49,50] All these oxidized Cu species are reduced to Cu^+ or Cu^0 situated at 932.2 eV in the spent sample,[28] accompanied by the disappearance of shake-up satellite peaks. For the Sm 3d spectra (Figure S21a) obtained from the catalyst surface, the peaks are attributed to the Sm^{3+}, which exists stably in the fresh and used samples. As to the C 1s spectra (Figure S21b), the

two peaks are assigned to the C−C bond and surface carbonates,[51] which is in line with the carbonate from $Sm_2O_2CO_3$. The status of Cu species is continuously explored through the in situ infrared spectra at −143 °C with CO adsorption on the $xCu/Sm_2O_2CO_3$ catalysts after H_2 pretreatment, which is shown in Figures 4f and S22. Based on the adsorption of CO on diverse Cu species reported in the literature, located at 2120−2140, 2100−2120, and 2000−2100 cm^{-1} are ascribed to Cu^{2+}, Cu^+, and Cu^0, respectively.[52−54] After the introduction of different pressures of CO, three CO bands at 2067/2071, 2090/2093, and 2172 cm^{-1} emerge for $5Cu/Sm_2O_2CO_3$ (Figure 4f) and $10Cu/Sm_2O_2CO_3$ (Figure S22) catalysts, which are assigned to the $CO−Cu^0$, $CO−Cu^+$, and $CO−Sm^{3+}$, respectively. The intensity of CO adsorption on Cu species increases with the increase of CO pressure, while the adsorption on Sm^{3+} decreases significantly with increasing the degree of vacuum to 1.0×10^{-7} mbar, indicating a weak $CO-Sm^{3+}$ bond energy. In situ infrared test reflects the coexistence of Cu^+ and Cu^0 in $xCu/Sm_2O_2CO_3$ samples after reduction pretreatment. Meanwhile, the significant desorption of CO during the process of N_2 purging (Figure S23) demonstrates that the CO is unable to block the surface sites. Furthermore, the MS signals of H_2 are recorded during the H_2-TPR process of the fresh and used $5Cu/Sm_2O_2CO_3$ samples, as displayed in Figure 4g, and the results demonstrated that the oxidized Cu species still present in the system after the in situ WGS reaction. Combining the above systematic characterizations, we explore the states of Cu species and the active sites of CO adsorption during the WGS reaction, respectively, and

confirm that Cu^+ and Cu^0 coexist during the reaction, but Cu^+ at the interface is the better reactive species.

After determining the adsorption and dissociation sites of CO and H_2O, we further analyze the dependence of the sample reactivity on the concentration of different reactants and product molecules in the WGS reaction by measuring the reaction order. As shown in Figure S24, we can see that the $5Cu/Sm_2O_2CO_3$ catalyst gives a higher absolute value of CO reaction order and a lower absolute value of H_2O and CO_2 reaction order compared with the $5Cu/Al_2O_3$ catalyst. This demonstrates that the surface of the $5Cu/Sm_2O_2CO_3$ catalyst has unsaturated CO, which will not cover the active sites, as well as the ability to dissociate H_2O and desorb CO_2 efficiently. In addition, the steady-state isotopic transient kinetic analysis (SSITKA) experiments shown in Figures S25– S28 show that the $5Cu/Sm_2O_2CO_3$ sample exhibits a lower surface coverage of CO_2 (θ_{CO_2}) and higher surface coverage of CO (θ_{CO}) compared with the $5Cu/Al_2O_3$ catalyst, demonstrating that H_2O molecules are relatively apt to replace generated CO_2 molecules under reaction conditions and that the desorption of CO_2 molecules is effective. This further confirms the exchange of H_2O and CO_2, as well as its positive role in promoting H_2O dissociation and CO_2 desorption and accelerating the WGS reaction.

3.4. WGS Reaction Mechanism Study. As an important industrial hydrogen production reaction, the mechanism of WGS reaction has always been the focus of attention. At present, two prominent mechanisms of WGS reaction for Cu-based catalysts have been proposed, the redox mechanism and the associative mechanism.[55,56] It is generally believed that the redox mechanism is that the CO molecules adsorbed on the surface of samples and reacted with the oxygen of the metal-oxide support to form CO_2, leading to the generation of the oxygen vacancies, which are responsible for the H_2O dissociation to produce hydrogen. Then, the two hydrogen atoms combined to form hydrogen gas.[14] In the associative mechanism, the adsorbed CO molecules reacted with the *OH derived from H_2O dissociation to form the intermediate, which immediately decomposed to generate CO_2 and H_2.[57,58] A TPSR test is conducted to check the mechanism followed by the $5Cu/Sm_2O_2CO_3$ sample for catalyzing the WGS reaction. Before verification, we created a realistic catalyst surface through the in situ WGS reaction at 300 °C (Figure 5a). In the calibration concentration curve of the WGS reaction process, the signal ratio of CO_2 to H_2 remains stable at 1, which is well in line with the ratio of the CO and H_2O reaction products ($CO + H_2O = CO_2 + H_2$). After that, the sample surface is cleaned under Ar gas to remove the gaseous H_2O molecules, and then H_2O is reintroduced separately to observe the H_2 signal. Within 30 min, no H_2 signal is detected (Figure 5b), making it clear that there is no redox mechanism. Continue to remove gaseous H_2O molecules below 300 °C in the Ar atmosphere, leaving only surface *OH. After lowering to RT, we switch to 2% CO/Ar for the reaction with *OH and observe the ratio of CO_2 and H_2 concentration in the outlet gas. To eliminate the influence of CO_2 generated by the decomposition of the support, the temperature rise is interrupted and started to maintain after 300 °C because the CO_2 signal appears in the sample after 300 °C from the experiment (Figure S20b) of temperature programming under Ar. Interestingly, the ratio of generated CO_2 and H_2 is perfectly preserved at 2 for 1 h at 300 °C (Figure 5c), proving the associative mechanism of the $5Cu/Sm_2O_2CO_3$ catalyst for

catalyzing the WGS reaction. The $20Cu/Sm_2O_2CO_3$ sample exhibits the same result, which is shown in Figure S29.

In addition, the DFT calculations are also performed to validate the WGS reaction mechanism. To simulate the composite catalyst, four Cu atoms are combined with the hydroxyl surface using the Cu−O bond, as shown in Figure 5d. The WGS reaction mechanism on the catalyst model is composed of eight elementary reactions, as shown in Figure 5e. The WGS reaction started with one CO adsorbed on the Cu cluster (IM1); then, the hydroxide radical on the catalyst surface migrates to the boundary between the Cu cluster and the hydroxyl surface (IM2). The subsequent elementary reaction happens with the formation of the C−O bond, namely, IM3. The first product, CO_2, is released while the Cu− C and Cu−O bonds are ruptured (IM4). The transient hydroxyl vacancy on the surface is unstable and inclined to capture water molecules (IM5). The adsorbed H_2O is decomposed into *OH and *H (IM6), and then, the *H combined with the H atom formed in the previous step and emitted H_2 (IM7). There are six spontaneous elementary reactions, and the other two reactions (the OH-migration and the H-migration, i.e., IM1 → IM2 and IM6 → IM7) have positive Gibbs energies of reaction. Despite the lower thermodynamic equilibrium ratios of IM2 and IM7, the WGS reaction occurs continuously on account of the Gibbs energy of the overall reaction, that is, −2.542 eV. In addition, DFT calculations accompanied by the very high Gibbs energies also exclude the redox mechanism (Table S8), which is in line with the results of experiment. Therefore, the associative mechanism is confirmed for $Cu/Sm_2O_2CO_3$ to catalyze the WGS reaction with the support of theoretical calculations and experiments. However, it is noteworthy that the calculations have their drawbacks. The molecular formula of the computational model is $Sm_{60}C_{24}O_{144}H_9Cu_4$, and the number of atoms to simulate is much less than that of real catalysts. This means that the simulation will inevitably be affected by the computing capabilities of quantum chemistry software and workstations. There are also limitations of accuracy, such as reducing the overestimated bond energies and increasing the bond lengths, using the method on account of the generalized gradient approximation. The imprecise mesh sampling of phonon frequency calculations can also cause deviations in the chemical potentials of catalysts. In summary, Cu^+ is in charge of CO adsorption, while $Sm_2O_2CO_3$ focuses on the dissociation of H_2O. Here, the adsorbed CO reacts with *OH to form CO_2 and H_2O, promoting the WGS reaction process. In addition, the system is successfully extended to Cu/ $La_2O_2CO_3$ catalysts, which exhibit similar properties to Cu/ $Sm_2O_2CO_3$, including the exchange capacity of CO_2 and H_2O on the catalyst surface, prominent WGS reactivity, and an associative mechanism for the WGS reaction (Figures S30– S32).

4. CONCLUSIONS

It is crucial to design and synthesize catalysts whose structures are conducive to the dissociation of the reactant molecules and the desorption of product molecules in the catalytic reactions, further promoting the equilibrium shift. Herein, the $Ln_2O_2CO_3$ (Ln = La and Sm) structure with an ordered arrangement of metal oxide $(Ln_2O_2)^{2+}$ and CO_3^{2-} layers is prepared by the simple hydrothermal method, and after loading the active metal Cu, it exhibits unexpected activity and excellent durability in the WGS reaction. An interesting phenomenon

is observed that the surface carbonate layer and hydroxyl can be interchanged and replenished by CO_2 and H_2O, respectively, which facilitates efficient cycling of the reaction and neatly solves the problem of carbonate accumulation and H_2O dissociation. The proposal of this layered structure containing metal oxide and carbonate provides vast and unforeseen opportunities for the application of rare-earth complex oxides in the field of catalysis.

■ ASSOCIATED CONTENT

ⓢ Supporting Information

The Supporting Information is available free of charge at https://pubs.acs.org/doi/10.1021/jacs.2c10326.

> Methods of simulation and experimental data, including catalytic reactivity, TEM, XRD, XPS, and in situ DRIFTS results (PDF)

■ AUTHOR INFORMATION

Corresponding Authors

Chun-Jiang Jia − *Key Laboratory for Colloid and Interface Chemistry, Key Laboratory of Special Aggregated Materials, School of Chemistry and Chemical Engineering, Shandong University, Jinan 250100, China;* ⓘ orcid.org/0000-0002-4254-5100; Email: jiacj@sdu.edu.cn

Feng Ryan Wang − *Department of Chemical Engineering, University College London, London WC1E 7JE, U.K.;* ⓘ orcid.org/0000-0002-2475-606X; Email: ryan.wang@ucl.ac.uk

Chun-Hua Yan − *Beijing National Laboratory for Molecular Sciences, State Key Lab of Rare Earth Materials Chemistry and Applications, PKU-HKU Joint Lab in Rare Earth Materials and Bioinorganic Chemistry, Peking University, Beijing 100871, China;* ⓘ orcid.org/0000-0002-0581-2951; Email: yan@pku.edu.cn

Authors

Lu-Lu Zhou − *Key Laboratory for Colloid and Interface Chemistry, Key Laboratory of Special Aggregated Materials, School of Chemistry and Chemical Engineering, Shandong University, Jinan 250100, China;* ⓘ orcid.org/0000-0002-0577-9805

Shan-Qing Li − *School of Materials and Environmental Engineering, Chizhou University, Chizhou 247000, China*

Chao Ma − *College of Materials Science and Engineering, Hunan University, Changsha 410082, China;* ⓘ orcid.org/0000-0001-8599-9340

Xin-Pu Fu − *Key Laboratory for Colloid and Interface Chemistry, Key Laboratory of Special Aggregated Materials, School of Chemistry and Chemical Engineering, Shandong University, Jinan 250100, China;* ⓘ orcid.org/0000-0001-8379-0789

Yi-Shuang Xu − *Key Laboratory for Colloid and Interface Chemistry, Key Laboratory of Special Aggregated Materials, School of Chemistry and Chemical Engineering, Shandong University, Jinan 250100, China;* ⓘ orcid.org/0000-0002-7066-0878

Wei-Wei Wang − *Key Laboratory for Colloid and Interface Chemistry, Key Laboratory of Special Aggregated Materials, School of Chemistry and Chemical Engineering, Shandong University, Jinan 250100, China;* ⓘ orcid.org/0000-0002-4471-2152

Hao Dong − *Beijing National Laboratory for Molecular Sciences, State Key Lab of Rare Earth Materials Chemistry and Applications, PKU-HKU Joint Lab in Rare Earth Materials and Bioinorganic Chemistry, Peking University, Beijing 100871, China;* ⓘ orcid.org/0000-0003-1007-1673

Complete contact information is available at:
https://pubs.acs.org/10.1021/jacs.2c10326

Author Contributions

All authors have given approval to the final version of the manuscript.

Notes

The authors declare no competing financial interest.

■ REFERENCES

(1) Tsai, C. H.; Chen, H. T.; Althaus, S. M.; Mao, K.; Kobayashi, T.; Pruski, M.; Lin, V. S. Y. Rational Catalyst Design: A Multifunctional Mesoporous Silica Catalyst for Shifting the Reaction Equilibrium by Removal of Byproduct. *ACS Catal.* **2011**, *1*, 729−732.

(2) Wei, L. Y.; Azad, H.; Haije, W.; Grenman, H.; de Jong, W. Pure methane from CO_2 hydrogenation using a sorption enhanced process with catalyst/zeolite bifunctional materials. *Appl. Catal. B: Environ.* **2021**, *297*, 120399.

(3) Huang, W. J.; Yu, C. T.; Sheu, W. J.; Chen, Y. C. The effect of non-uniform temperature on the sorption-enhanced steam methane reforming in a tubular fixed-bed reactor. *Int. J. Hydrogen Energ.* **2021**, *46*, 16522−16533.

(4) Tian, S. C.; Yan, F.; Zhang, Z. T.; Jiang, J. G. Calcium-looping reforming of methane realizes in situ CO_2 utilization with improved energy efficiency. *Sci. Adv.* **2019**, *5*, No. eaav5077.

(5) Wang, H.; Wang, L.; Lin, D.; Feng, X.; Niu, Y. M.; Zhang, B. S.; Xiao, F. S. Strong metal−support interactions on gold nanoparticle catalysts achieved through Le Chatelier's principle. *Nat. Catal.* **2021**, *4*, 418−424.

(6) Buelens, L. C.; Galvita, V. V.; Poelman, H.; Detavernier, C.; Marin, G. B. Super-dry reforming of methane intensifies CO_2 utilization via Le Chatelier's principle. *Science* **2016**, *354*, 449−452.

(7) Ge, Y. Z.; Qin, X. T.; Li, A.; Deng, Y. C.; Lin, L. L.; Zhang, M. T.; Yu, Q. L.; Li, S. W.; Peng, M.; Xu, Y.; Zhao, X. Y.; Xu, M. Q.; Zhou, W.; Yao, S. Y.; Ma, D. Maximizing the Synergistic Effect of CoNi Catalyst on α-MoC for Robust Hydrogen Production. *J. Am. Chem. Soc.* **2021**, *143*, 628−633.

(8) Yao, S. Y.; Zhang, X.; Zhou, W.; Gao, R.; Xu, W. Q.; Ye, Y. F.; Lin, L. L.; Wen, X. D.; Liu, P.; Chen, B. B.; Crumlin, E.; Guo, J. H.; Zuo, Z. J.; Li, W. Z.; Xie, J. L.; Lu, L.; Kiely, J.; Shi, L.; Rodriguez, C.; Ma, J. A.; Ma, D. Atomic-layered Au clusters on α-MoC as catalysts for the low-temperature water-gas shift reaction. *Science* **2017**, *357*, 389−393.

(9) Wei, S.; Wang, W. W.; Fu, X. P.; Li, S. Q.; Jia, C. J. The effect of reactants adsorption and products desorption for Au/TiO_2 incatalyzing CO oxidation. *J. Catal.* **2019**, *376*, 134−145.

(10) Lin, J.; Wang, A. Q.; Qiao, B. T.; Liu, X. Y.; Yang, X. F.; Wang, X. D.; Liang, J. X.; Li, J.; Liu, J. Y.; Zhang, T. Remarkable Performance of Ir_1/FeO_x Single-Atom Catalyst in Water Gas Shift Reaction. *J. Am. Chem. Soc.* **2013**, *135*, 15314−15317.

(11) Zhu, M. H.; Rocha, T.; Lunkenbein, T.; Knop-Gericke, A.; Schlögl, R.; Wachs, I. E. Promotion Mechanisms of Iron Oxide-Based High Temperature Water—Gas Shift Catalysts by Chromium and Copper. *ACS Catal.* **2016**, *6*, 4455—4464.

(12) Yan, H.; Yang, C.; Shao, W. P.; Cai, L. H.; Wang, W. W.; Jin, Z.; Jia, C. J. Construction of stabilized bulk-nano interfaces for highly promoted inverse CeO$_2$/Cu catalyst. *Nat. Commun.* **2019**, *10*, 3470.

(13) Zhang, X.; Zhang, M. T.; Deng, Y. C.; Xu, M. Q.; Artiglia, L. W.; Wen, R.; Gao, B. B.; Chen, S. Y.; Yao, X. C.; Zhang, M.; Peng, J.; Yan, A. W.; Li, Z.; Jiang, X. Y.; Gao, S. F.; Cao, C.; Yang, A. J.; Kropf, J. N.; Shi, J. L.; Xie, M. S.; Bi, J. A.; van Bokhoven, Y. W.; Li, X. D.; Wen, M.; Flytzani-Stephanopoulos, C.; Shi, W.; Zhou, D.; Ma, D. A stable low-temperature H$_2$-production catalyst by crowding Pt on α-MoC. *Nature* **2021**, *589*, 396—401.

(14) Gokhale, A. A.; Dumesic, J. A.; Mavrikakis, M. On the Mechanism of Low-Temperature Water Gas Shift Reaction on Copper. *J. Am. Chem. Soc.* **2008**, *130*, 1402—1414.

(15) Liu, N.; Xu, M.; Yang, Y. S.; Zhang, S. M.; Zhang, J.; Wang, W. L.; Zheng, L. R.; Hong, S.; Wei, M. Au$^{\delta-}$—O$_v$—Ti^{3+} Interfacial Site: Catalytic Active Center toward Low Temperature Water Gas Shift Reaction. *ACS Catal.* **2019**, *9*, 2707—2717.

(16) Fu, X. P.; Guo, L. W.; Wang, W. W.; Ma, C.; Jia, C. J.; Wu, K.; Si, R.; Sun, L. D.; Yan, C. H. Direct Identification of Active Surface Species for the Water—Gas Shift Reaction on a Gold—Ceria Catalyst. *J. Am. Chem. Soc.* **2019**, *141*, 4613—4623.

(17) Chen, A.; Yu, X. J.; Zhou, Y.; Miao, S.; Li, Y.; Kuld, S.; Sehested, J.; Liu, J. Y.; Aoki, T.; Hong, S.; Camellone, M. F.; Fabris, S.; Ning, J.; Jin, C. C.; Yang, C. W.; Nefedov, A.; Wöll, C.; Wang, Y. M.; Shen, W. J. Structure of the catalytically active copper—ceria interfacial perimeter. *Nat. Catal.* **2019**, *2*, 334—341.

(18) Zhu, M. H.; Tian, P. F.; Kurtz, R.; Lunkenbein, T.; Xu, J.; Schlögl, R.; Wachs, I. E.; Han, Y. F. Strong Metal—Support Interactions between Copper and Iron Oxide during the High-Temperature Water-Gas Shift Reaction. *Angew. Chem., Int. Ed.* **2019**, *58*, 9083—9087.

(19) Panagiotopoulou, P.; Kondarides, D. I. Effects of promotion of TiO$_2$ with alkaline earth metals on the chemisorptive properties and water—gas shift activity of supported platinum catalysts. *Appl. Catal. B: Environ.* **2011**, *101*, 738—746.

(20) Jacobs, G.; Graham, U. M.; Chenu, E.; Patterson, P. M.; Dozier, A.; Davis, B. H. Low-temperature water—gas shift: impact of Pt promoter loading on the partial reduction of ceria and consequences for catalyst design. *J. Catal.* **2005**, *229*, 499—512.

(21) Djinović, P.; Batista, J.; Levec, J.; Pintar, A. Comparison of water—gas shift reaction activity and long-term stability of nano-structured CuO-CeO$_2$ catalysts prepared by hard template and co-precipitation methods. *Appl. Catal. A: Gen.* **2009**, *364*, 156—165.

(22) Cornaglia, C. A.; Múnera, J. F.; Cornaglia, L. M.; Lombardo, E. A.; Ruiz, P.; Karelovic, A. Effect of the support on the catalytic stability of Rh formulations for the water—gas shift reaction. *Appl. Catal. A: Gen.* **2012**, *435—436*, 99—106.

(23) Watson, C. D.; Martinelli, M.; Cronauer, D. C.; Kropf, A. J.; Jacobs, G. Low Temperature Water-Gas Shift: Enhancing Stability through Optimizing Rb Loading on Pt/ZrO$_2$. *Catalysts* **2021**, *11*, 210.

(24) Suzuki, T.; Sackmann, A.; Oprea, A.; Weimar, U.; Bârsan, N. Chemoresistive CO$_2$ Gas Sensors Based on La$_2$O$_2$CO$_3$: Sensing Mechanism Insights Provided by Operando Characterization. *ACS Sens* **2020**, *5*, 2555—2562.

(25) Wang, H. B.; Qian, C.; Yi, Z. G.; Rao, L.; Liu, H. R.; Zeng, S. J. Hydrothermal Synthesis and Tunable Multicolor Upconversion Emission of Cubic Phase Y$_2$O$_3$ Nanoparticles. *Adv. Cond. Matter. Phys.* **2013**, *2013*, 347406.

(26) Mai, H. X.; Sun, L. D.; Zhang, Y. W.; Si, R.; Feng, W.; Zhang, H. P.; Liu, H. C.; Yan, C. H. Shape-Selective Synthesis and Oxygen Storage Behavior of Ceria Nanopolyhedra, Nanorods, and Nano-cubes. *J. Phys. Chem. B* **2005**, *109*, 24380—24385.

(27) Yu, W. Z.; Fu, X. P.; Xu, K.; Ling, C.; Wang, W. W.; Jia, C. J. CO$_2$ methanation catalyzed by a Fe-Co/Al$_2$O$_3$ catalyst. *J. Environ. Chem. Eng.* **2021**, *9*, 105594.

(28) Si, R.; Raitano, J.; Yi, N.; Zhang, L. H.; Chan, S. W.; Flytzani-Stephanopoulos, M. Structure sensitivity of the low-temperature water-gas shift reaction on Cu—CeO$_2$ catalysts. *Catal. Today* **2012**, *180*, 68—80.

(29) Kresse, G.; Hafner, J. Ab. initio molecular dynamics for liquid metals. *Phys. Rev. B* **1993**, *47*, 558—561.

(30) Kresse, G.; Furthmüller, J. Efficient iterative schemes for ab initio total-energy calculations using a plane-wave basis set. *Phys. Rev. B* **1996**, *54*, 11169—11186.

(31) Perdew, J. P.; Burke, K.; Ernzerhof, M. Generalized Gradient Approximation Made Simple. *Phys. Rev. Lett.* **1996**, *77*, 3865—3868.

(32) Blöchl, P. E. Projector augmented-wave method. *Phys. Rev. B* **1994**, *50*, 17953—17979.

(33) Razali, N.; McGregor, J. Improving Product Yield in the Direct Carboxylation of Glycerol with CO$_2$ through the Tailored Selection of Dehydrating Agents. *Catalysts* **2021**, *11*, 138.

(34) Ziemba, M.; Weyel, J.; Hess, C. Elucidating the mechanism of the reverse water—gas shift reaction over Au/CeO$_2$ catalysts using operando and transient spectroscopies. *Appl. Catal. B: Environ.* **2022**, *301*, 120825.

(35) Kang, L. Q.; Wang, B.; Güntner, A. T.; Xu, S. Y.; Wan, X. H.; Liu, Y. Y.; Marlow, S.; Ren, Y. F.; Gianolio, D.; Tang, C. C.; Murzin, V.; Asakura, H.; He, Q.; Guan, S. L.; Velasco-Vélez, J. J.; Pratsinis, S. E.; Guo, Y. Z.; Wang, F. R. The Electrophilicity of Surface Carbon Species in the Redox Reactions of CuO-CeO$_2$ Catalysts. *Angew. Chem., Int. Ed.* **2021**, *60*, 14420—14428.

(36) Tepamatr, P.; Laosiripojana, N.; Charojrochkul, S. Water gas shift reaction over monometallic and bimetallic catalysts supported by mixed oxide materials. *Appl. Catal. A. Gen.* **2016**, *523*, 255—262.

(37) Jin, S.; Park, Y.; Bang, G.; Vo, N. D.; Lee, C. H. Revisiting magnesium oxide to boost hydrogen production via water-gas shift reaction: Mechanistic study to economic evaluation. *Appl. Catal. B: Environ.* **2021**, *284*, 119701.

(38) Chen, Y. Q.; Li, X. G.; Li, J.; Wu, L. P.; Li, X. J. Cu nanoparticles confined in TiO$_2$ nanotubes to enhance the water-gas shift reaction activity. *Int. J. Green Energy* **2021**, *18*, 595—601.

(39) García-Moncada, N.; González-Castaño, M.; Ivanova, S.; Centeno, M. Á.; Romero-Sarria, F.; Odriozola, J. A. New concept for old reaction: Novel WGS catalyst design. *Appl. Catal. B: Environ.* **2018**, *238*, 1—5.

(40) Zhu, M. H.; Yalçın, Ö.; Wachs, I. E. Revealing structure-activity relationships in chromium free high temperature shift catalysts promoted by earth abundant elements. *Appl. Catal. B: Environ.* **2018**, *232*, 205—212.

(41) Gawade, P.; Mirkelamoglu, B.; Ozkan, U. S. The Role of Support Morphology and Impregnation Medium on the Water Gas Shift Activity of Ceria-Supported Copper Catalysts. *J. Phys. Chem. C* **2010**, *114*, 18173—18181.

(42) Wu, H. C.; Chen, T. C.; Wu, J. H.; Chen, C. H.; Lee, J. F.; Chen, C. S. The effect of an Fe promoter on Cu/SiO$_2$ catalysts for improving their catalytic activity and stability in the water-gas shift reaction. *Catal. Sci. Technol.* **2016**, *6*, 6087.

(43) Chen, C. Q.; Zhan, Y. Y.; Zhou, J. K.; Li, D. L.; Zhang, Y. J.; Lin, X. Y.; Jiang, L. L.; Zheng, Q. Cu/CeO$_2$ Catalyst for Water-Gas Shift Reaction: Effect of CeO$_2$ Pretreatment. *ChemPhysChem* **2018**, *19*, 1448—1455.

(44) Lang, Y.; Du, C.; Tang, Y. T.; Chen, Y. J.; Zhao, Y. K.; Chen, R.; Liu, X.; Shan, B. Highly efficient copper-manganese oxide catalysts with abundant surface vacancies for lowtemperature water-gas shift reaction. *Int. J. Hydrogen Energ.* **2020**, *45*, 8629—8639.

(45) Koryabkina, N. A.; Phatak, A. A.; Ruettinger, W. F.; Farrauto, R. J.; Ribeiro, F. H. Determination of kinetic parameters for the water—gas shift reaction on copper catalysts under realistic conditions for fuel cell applications. *J. Catal.* **2003**, *217*, 233—239.

(46) Yu, Z. Y.; Zhang, Z. H.; Zhang, Y. S.; Huang, W. X. Titania Morphology-Dependent Catalysis of CuO$_x$/TiO$_2$ Catalysts in CO Oxidation and Water Gas Shift Reactions. *ChemCatChem* **2020**, *12*, 3679—3686.

(47) Li, Y.; Fu, Q.; Flytzani-Stephanopoulos, M. Low-temperature water-gas shift reaction over Cu- and Ni-loaded cerium oxide catalysts. *Appl. Catal. B: Environ.* **2000**, *27*, 179−191.

(48) Xie, X. W.; Li, Y.; Liu, Z. Q.; Haruta, M.; Shen, W. J. Low-temperature oxidation of CO catalysed by Co_3O_4 nanorods. *Nature* **2009**, *458*, 746−749.

(49) Zeng, D. W.; Yung, K. C.; Xie, C. S. UV Nd:YAG laser ablation of copper: chemical states in both crater and halo studied by XPS. *Appl. Surf. Sci.* **2003**, *217*, 170−180.

(50) Gaudin, P.; Fioux, P.; Dorge, S.; Nouali, H.; Vierling, M.; Fiani, E.; Molière, M.; Brilhac, J. F.; Patarin, J. Formation and role of Cu^+ species on highly dispersed CuO/SBA-15 mesoporous materials for SO_x removal: An XPS study. *Fuel Process. Technol.* **2016**, *153*, 129−136.

(51) Jin, S.; Shao, W.; Chen, S. C.; Li, L.; Shang, S.; Zhao, Y.; Zhang, X. D.; Xie, Y. Ultrathin In-Plane Heterostructures for Efficient CO_2 Chemical Fixation. *Angew. Chem., Int. Ed.* **2022**, *61*, No. e202113411.

(52) Chen, S. Z.; Zou, H. B.; Liu, Z. L.; Lin, W. M. DRIFTS study of different gas adsorption for CO selective oxidation on Cu−Zr−Ce−O catalysts. *Appl. Surf. Sci.* **2009**, *255*, 6963−6967.

(53) Kydd, R.; Ferri, D.; Hug, P.; Scott, J.; Teoh, W. Y.; Amal, R. Temperature-induced evolution of reaction sites and mechanisms during preferential oxidation of CO. *J. Catal.* **2011**, *277*, 64−71.

(54) Liu, H. X.; Li, S. Q.; Wang, W. W.; Yu, W. Z.; Zhang, W. J.; Ma, C.; Jia, C. J. Partially sintered copper−ceria as excellent catalyst for the high-temperature reverse water gas shift reaction. *Nat. Commun.* **2022**, *13*, 867.

(55) Kalamaras, C. M.; Americanou, S.; Efstathiou, A. M. Redox" vs "associative formate with −OH group regeneration" WGS reaction mechanism on Pt/CeO_2: Effect of platinum particle size. *J. Catal.* **2011**, *279*, 287−300.

(56) Baraj, E.; Ciahotný, K.; Hlinčík, T. The water gas shift reaction: Catalysts and reaction mechanism. *Fuel* **2021**, *288*, 119817.

(57) Yu, W. Z.; Wang, W. W.; Ma, C.; Li, S. Q.; Wu, K.; Zhu, J. Z.; Zhao, H. R.; Yan, C. H.; Jia, C. J. Very high loading oxidized copper supported on ceria to catalyze the water-gas shift reaction. *J. Catal.* **2021**, *402*, 83−93.

(58) Xu, K.; Ma, C.; Yan, H.; Gu, H.; Wang, W. W.; Li, S. Q.; Meng, Q. L.; Shao, W. P.; Ding, G. H.; Wang, F. R.; Jia, C. J. Catalytically efficient Ni-NiO_x-Y_2O_3 interface for medium temperature water-gas shift reaction. *Nat. Commun.* **2022**, *13*, 2443.